Unlocking anionic redox activity in O3-type sodium 3d layered oxides via Li substitution

Qing Wang, Sathiya Mariyappan, Gwenaëlle Rousse, Anatolii Morozov, Benjamin Porcheron, Rémi Dedryvère, Jinpeng Wu, Wanli Yang, Leiting Zhang, Mohamed Chakir, et al.

Unlocking anionic redox activity in O3-type sodium 3*d* layered oxides via Li substitution

Qing Wang[1,2,3], Sathiya Mariyappan[1,4], Gwenaëlle Rousse[1,2,4], Anatoly V. Morozov[5], Benjamin Porcheron[6], Rémi Dedryvère[4,7], Jinpeng Wu[8], Wanli Yang[8], Leiting Zhang[9], Mohamed Chakir[3], Maxim Avdeev[10,11], Michaël Deschamps[6], Young-Sang Yu[8], Jordi Cabana[12], Marie-Liesse Doublet[4,13], Artem M. Abakumov[5], and Jean-Marie Tarascon[1,2,4,*]

[1]*Chimie du Solide-Energie, UMR 8260, Collège de France, 75231 Paris Cedex 05, France*
[2]*Sorbonne Université, 4 Place Jussieu, 75005, Paris, France*
[3]*Renault, Technocentre, 1 avenue du Golf, 78288 Guyancourt, France*
[4] *Réseau sur le Stockage Electrochimique de l'Energie (RS2E), FR CNRS 3459, France*
[5]*Center for Energy Science and Technology, Skolkovo Institute of Science and Technology, Nobel str. 3, 143026 Moscow, Russia*
[6]*CNRS, CEMHTI UPR3079, Université d'Orléans, 1D avenue de la recherche scientifique, 45071 Orléans Cedex 2, France*
[7]*IPREM-UMR 5254 CNRS, Université de Pau et des Pays de l'Adour, Hélioparc, 2 Avenue Pierre Angot, 64053 Pau Cedex 9, France*
[8]*Advanced Light Source, Lawrence Berkeley National Laboratory, One Cyclotron Road, Berkeley, CA 94720, USA*
[9]*Electrochemistry Laboratory, Paul Scherrer Institute, Forschungsstrasse 111, 5232, Villigen PSI, Switzerland*
[10]*School of Chemistry, The University of Sydney, Sydney, NSW 2006, Australia*
[11]*Australian Centre for Neuron Scattering, Australian Nuclear Science and Technology Organisation, Locked Bag 2001, Kirrawee DC, NSW 2232, Australia*
[12]*University of Illinois at Chicago, Department of Chemistry, Chicago Illinois 60607, United States*
[13]*ICGM, Univ. Montpellier, CNRS, ENSCM, Montpellier, France.*
.
*Corresponding author: jean-marie.tarascon@college-de-france.fr

Keywords: Na-ion batteries, O3-type layered oxide, water-stable, anionic redox, cation migration

Abstract

Sodium ion batteries, because of their sustainability attributes, could be an attractive alternative to Li-ion technology for specific applications. However, it remains challenging to design high energy density and moisture stable Na-based positive electrodes by implementing the anionic redox process that has recently boosted the capacity of Li-rich layered oxides. Here, we report the first anionic-redox active O3-$NaLi_{1/3}Mn_{2/3}O_2$ phase obtained through a ceramic process by carefully controlling the delicate balance between synthesis conditions and stoichiometry. It shows a sustained reversible capacity of 190 mAh g^{-1} by redox processes on oxygen and manganese ions as deduced by combined HAXPES and mRIXS spectroscopy techniques. Remarkably, unlike any other anionic-redox layered oxides so far

reported, O3-$NaLi_{1/3}Mn_{2/3}O_2$ electrodes do not show voltage fade upon cycling. This finding is due to switching from the interlayer to intralayer migration of the Mn cations promoted by Li^+ displacement towards the alkali layer upon first Na^+ de-insertion. Another practical asset of this material stems from its moisture stability, hence facilitating its handling and electrode processing. Besides providing insightful fundamental findings pertaining to anion redox, this work offers future directions towards designing high energy density electrodes for advanced Na-ion batteries.

Introduction

Rechargeable lithium ion batteries have empowered the success of consumer devices, and are continuing to conquer the market of electric vehicles.[1] Despite the foreseeable dominance of Li-ion technology within the near future, there is a rising demand for cost-effective and more sustainable cathode materials for large-scale energy storage. The Na-ion technology, the working principle of which mimics Li-ion batteries, offers an alternative to fill this gap, provided improvements are made in terms of energy density.[2,3] Inspired by the discovery of anionic redox in Li-rich oxides with subsequent increase in the material capacity,[4–6] great efforts have been devoted to the design of Na-rich layered oxides ($Na(Na_yM_{1-y})O_2$, $0 < y < 1$, M = transition metal cation(s)). Commonly, anionic redox in layered oxides is triggered by the introduction of alkali metals into the $MO_2^{\delta-}$ layer that generates oxygen lone pairs associated with oxygen non-bonding 2*p*-states in the electronic structure.[7,8] However, implementing this strategy to Na layered oxides is not simple owing to the size mismatch between NaO_6 and MO_6 octahedra. Hence, Na-rich layered oxides with the O3-type structure were successfully prepared with either larger and more covalent 4*d* and/or 5*d* metals (Ru, Ir, etc.).[9–13] But with 3*d* metals, anionic redox is solely reported with non-stoichiometric P2/P3-type $Na_xA_yM_{1-y}O_2$ ($0 < x < 1$, $y < 1$) phases where the non-bonding O 2*p* orbitals are made available by increasing the O/M ratio compared to $LiMO_2$ using Li^+ / Mg^{2+} / Zn^{2+} or vacancies as the A cation instead of Na^+.[14–20] However, practical wise P2/P3 phases fall short in achieving high energy density target, because of their Na deficiency.[21] Hence, the standing challenge resides in the synthesis of anionic-redox active sodium layered oxides consisting of 3*d* transition metals while having full sodium stoichiometry ($Na(A,M)O_2$ with Na/(A,M) = 1).

Several attempts to increase the Na content have invariably led to anionic redox inactive O3-type structures which are thermodynamically favored against the P2 structure when Na/(A,M) ratio approaches 1.[22] This failure is most probably due to synthesis difficulties in achieving the proper targeted composition.[23–25] Combining the proper Li

content to trigger anionic redox with full Na occupancy has even been predicted by DFT and confirmed experimentally since the authors synthesized P2-$Na_{0.75}Li_{0.25}Mn_{0.75}O_2$ and not $NaLi_{1/3}Mn_{2/3}O_2$ as they wished .[26]

Following our early study on stabilizing the $NaLi_{1/3}Ir_{2/3}O_2$ phase,[27] we herein explore the delicate Na-Li composition balance in the $NaLi_yMn_{1-y}O_2$ phase to stabilize anionic-redox active O3 structure with full Na content and successfully synthesized a new $NaLi_{1/3}Mn_{2/3}O_2$ phase. It delivers an abnormally high first charge capacity of ~ 250 mAh g^{-1} with reversible capacity of ~190 mAh g^{-1} while showing neither voltage fade nor reactivity against moisture, both of which are serious assets practical-wise.

Identifying structure and composition of $NaLi_{1/3}Mn_{2/3}O_2$

A survey of various key parameters (Li/Mn ratio, nature of precursors, annealing temperature, flushing gases) was conducted and the results are cumulated in Supplementary Fig. 1−3 with the optimized synthesis condition explained in experimental section. Single phase was solely obtained for the composition $NaLi_{1/3}Mn_{2/3}O_2$ by heating a ball-milled mixture of Na_2O_2, Li_2O, and Mn_2O_3 at 700 °C in a tubular furnace, where the tube was flushed with argon before calcination. The X-ray powder diffraction (XRD) pattern of the as-synthesized material was fitted in an O3-type structure with minute amounts of an impurity phase (Supporting Fig. 1 and 4). Interestingly, by soaking the sample into distilled water, the impurity phase was washed away while leaving the O3 phase intact, hence indicating its stability against moisture (Supplementary Fig. 4 and 5). This water-washed material with a $Na_{0.97}Li_{0.32}Mn_{0.68}O_2$ composition deduced from inductively coupled plasma (ICP) analysis was further used for all studies and hereafter referred to as "$Na_1Li_{1/3}Mn_{2/3}O_2$" for simplicity purpose.

Figure 1a shows the synchrotron XRD (SXRD) pattern of the water-washed material. It can be refined using two models, both suitable for describing an O3 structure: either in the $R\bar{3}m$ space group with the lattice parameters a = 2.92441(1) Å, c = 15.96473(9) Å (Supplementary Fig. 6, Supplementary Table 1), or in the $C2/m$ space group with a = 5.05911(5) Å, b = 8.77505(6) Å, c = 5.58491(5) Å, and β = 107.6217(5)° (Fig. 1a, Supplementary Table 2). The latter indexes the superstructure reflections between 5−10° 2θ (Supplementary Fig. 6) that were not taken into account using the $R\bar{3}m$ space group and allows to describe the $[Li_{1/3}Mn_{2/3}]O_2$ honeycomb-ordered layers. In this model, Na is distributed in the interlayer space on two Wyckoff sites, 2c and 4h. The superstructure reflections shows asymmetric broadening and reduced intensities that arise from copious stacking faults as we deduced from simulated X-ray diffraction patterns (Supplementary Fig. 7), with these faults propagating

along the *c* axis,[9,11] as evidenced by [$\bar{1}$10] HAADF-STEM image (Fig. 1b) and corresponding SAED pattern (Supplementary Fig. 7). Both SXRD and STEM support the structure model where Na takes up octahedral sites in between the $[Li_{1/3}Mn_{2/3}]O_2$ slabs while Li and Mn form a "honeycomb" ordering within the $[Li_{1/3}Mn_{2/3}]O_2$ slabs. Lastly the neutron powder diffraction (NPD) was also collected for the pristine phase (Fig.1c, Supplementary Table 3) and alike XRD it is consistent with the target composition as deduced by the Rietveld refinement.

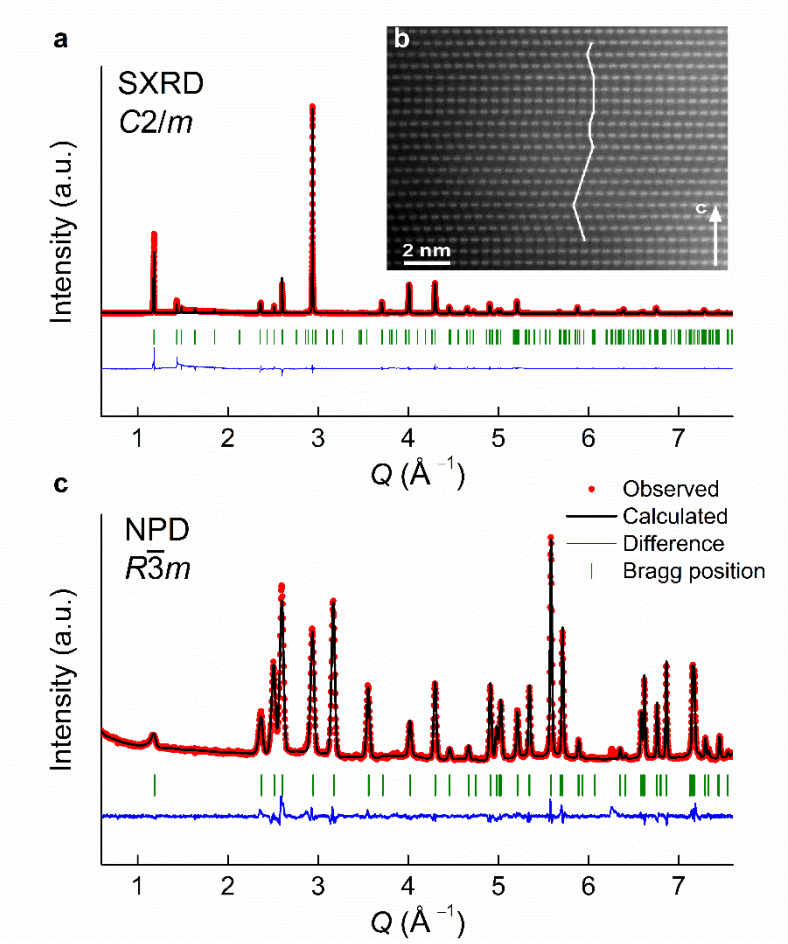

Fig. 1 Structure of the water-washed pristine material. a, Rietveld refinement of the SXRD pattern in *C*2/*m* space group (O3-type) of $NaLi_{1/3}Mn_{2/3}O_2$ after being washed in H_2O. The red dots, black, and blue lines and green tick bars represent the observed, calculated, difference patterns and Bragg positions, respectively. **b**, [$\bar{1}$10] HAADF-STEM image of pristine $NaLi_{1/3}Mn_{2/3}O_2$ (indexes refer to the *R*$\bar{3}$*m* cell). The periodicity along the stacking direction of the "honeycomb" $Li_{1/3}Mn_{2/3}O_2$ layers is frequently violated by stacking faults appearing as lateral shifts of the layers (traced with the white line). **c**, Rietveld refinement of the NPD pattern of H_2O-washed $NaLi_{1/3}Mn_{2/3}O_2$ sample. The *R*$\bar{3}$*m* space group was chosen instead of *C*2/*m* to fit the neutron pattern due to the bare visibility of superstructure peaks from the $[Li_{1/3}Mn_{2/3}]O_2$ honeycomb ordering. As the coherent neutron scattering lengths for Mn and Li differ only by a factor of 2 (*b* (Mn) = −0.37 fm versus *b* (Li) = −0.19 fm) as compared to a factor of 8 for XRD (*Z* (Mn) = 25 versus *Z* (Li) = 3), superstructure peaks

associated with the honeycomb ordering are barely visible in the NPD pattern than in XRD, and even more attenuated in presence of stacking faults.

Electrochemical properties of $NaLi_{1/3}Mn_{2/3}O_2$

The electrochemical properties of $NaLi_{1/3}Mn_{2/3}O_2$ were examined versus metallic Na within the voltage range of 1.5−4.5 V at the rate of C/8 (1C = 285 mAh g^{-1}) in Swagelok-type cells (Fig. 2). Upon oxidation, the voltage rapidly reaches a plateau at around 3.6 V followed by a sloping region to reach the "$Na_{0.09}Li_{1/3}Mn_{2/3}O_2$" composition at 4.5 V. The subsequent discharge profile evolves into a nearly S-shape curve, which persists upon repeated cycles, indicating an electrochemically driven structural transformation during the first charge. Out of 0.9 Na^+ that can be removed during the first charge, solely 0.67 Na^+ is reinserted on the following discharge without any loss of Li from the structure as deduced from inductively coupled plasma-optical emission spectrometry (ICP-OES) measurements performed on the fully charged and discharged samples (Supplementary Fig. 8). This leads to a reversible capacity of ~190 mAh g^{-1} which is stable upon continuous cycling, retaining 90% of the initial capacity after 40 cycles (Fig. 2a, inset). Similar behavior with charge activation and S-shaped curve evolution is usually observed for numerous anionic redox compounds[28] which occasionally show O_2 release. To check this possibility, we carried out pressure test and online electrochemical mass spectrometry (OEMS) (Fig. 2b, Supplementary Fig. 9). Both techniques confirm gas release in the first charge which is predominantly O_2 with the onset at ~0.58 Na^+ removal (*ca.* 3.8 V *vs.* Na^+/Na^0) as shown by OEMS data in Fig. 2b. For precise quantification, the OEMS analyses were carried out using $Na_3V_2(PO_4)_3$ (NVP) as counter electrode instead of sodium metal which itself generates gases by reactions with the electrolyte. Correspondingly, the amount of O_2 release in the first cycle equals to 757.4 µmol g^{-1} (equivalent to 80 mAh g^{-1} charge capacity, Fig. 2b), yielding the material composition $Na_{\sim 0.09}Li_{1/3}Mn_{2/3}O_{1.86}$ at the end of charge, whereas almost no O_2 release (less than 1%) is observed in the second charge. This irreversible O_2 release explains part of the first cycle irreversible capacity, and is likely rooted in the number of hole per oxygen (h^O) generated upon charge since this parameter was recently proposed as a good indicator of the reversibility of the anionic process.[8] Lastly, the CO_2 evolution observed through both cycles, as already being noticed with other layered oxides, is most likely linked with the decomposition of residual carbonates[29] on the material surface and/or from the oxidative decomposition of the electrolyte.[30] Through parallel measurements (Supplementary Fig.9)[31] we could conclude that the occurrence of CO_2 through the second cycling is likely associated

with the presence of H^+ generated by electrolyte decomposition as previously reported[32], which cannot be reduced using an NVP anode as opposed to a hard carbon or Na anode.

Altogether, the cycling profile and the O_2 gas release in the first cycle are reminiscent of Li-rich layered oxide. However, a striking difference emerges with the neatly superposition of the discharge curves upon cycling (Fig. 2c). This indicates the absence of noticeable voltage fade in $NaLi_{1/3}Mn_{2/3}O_2$ that we further confirmed by plotting the average discharge voltage for the first 40 cycles that remains constant (Fig. 2c, inset). Interestingly, such a feature is not mirrored in charge, which shows a gradual evolution in the shape of the charge curve on repeated cycling (Supplementary Fig. 10).

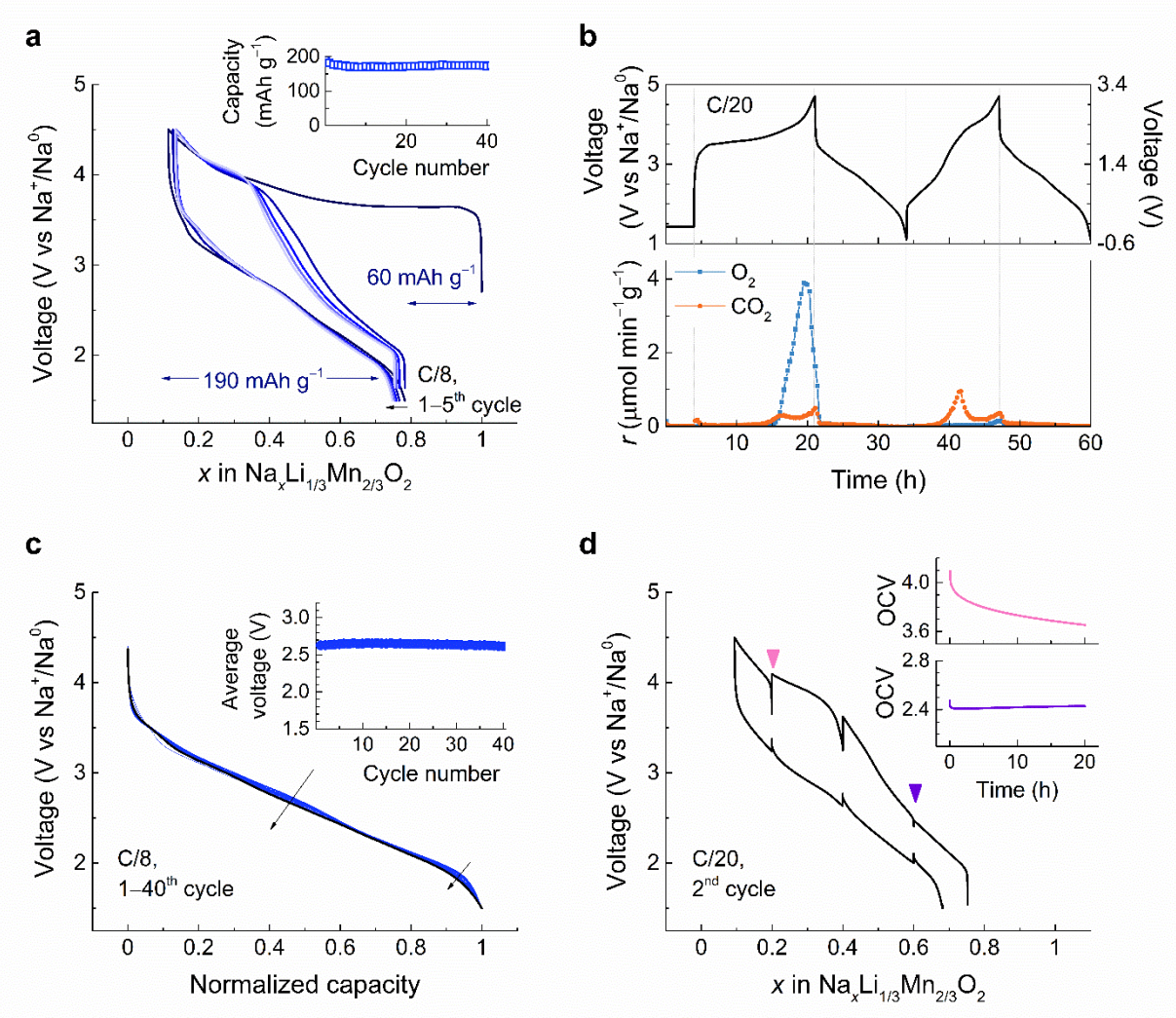

Figure 2 Electrochemical behavior of $NaLi_{1/3}Mn_{2/3}O_2$. a, Voltage profile of first five galvanostatic cycles (dark to light blue) of $NaLi_{1/3}Mn_{2/3}O_2$ against metallic sodium at C/8 rate between 1.5−4.5 V. Inset shows the capacity retention over 40 cycles. **b**, OEMS gas analysis during the first and second cycles of $NaLi_{1/3}Mn_{2/3}O_2$ cycled versus $Na_3V_2(PO_4)_3$ between −0.5−3.1 V (right axis), which is converted to 1.2−4.7 V vs Na^+/Na^0 (left axis) as presented in the upper panel. Gas evolution rates ($\mu mol.min^{-1}.g^{-1}$) were monitored for O_2 (m/z = 32) and CO_2 (m/z = 44) as shown in the bottom panel and the amount of O_2 release in the first cycle equals to 757.4 µmol g^{-1} (equivalent to 80 mAh g^{-1}

charge capacity). **c**, Normalized discharge curves of the $NaLi_{1/3}Mn_{2/3}O_2$/Na half cell data shown in Fig. 2a for 40 cycles. Inset shows the average discharge voltage calculated by dividing the specific energy by capacity omitting the *iR* drop upon cycling. **d**, GITT measurements conducted on the second cycle at a current rate of C/20, with a 20-hour relaxation period for every 4 hours (0.2 Na^+ exchange). Inset shows OCV evolution during 20 hours' relaxation at weakly and highly charged states.

To understand the asymmetric behavior between charge/discharge, we followed the variation of equilibrium potential process by galvanostatic intermittent titration technique (GITT). The GITT voltage profile for the second cycle (Fig. 2d) shows a large voltage gap (300 ~ 500 mV) between OCVs at charge vs. discharge despite very long rest periods of 20 hours. This suggests that the hysteresis is of thermodynamic nature. The comparison between the GITT measurements and a cell cycling at C/50 rate (Supplementary Fig. 11) also suggests slow equilibration dynamics. To better understand the hysteresis, we progressively opened the charge window with each cycle by increasing the upper cut-off voltage (Supplementary Fig. 12). Charge profiles are identical but discharge profiles drop gradually upon reaching the high voltage redox process (> 3.3 V) with simultaneous rapid growth of the overpotential, therefore pointing that the hysteresis is triggered towards the last 50% of charge. Moreover, the magnification of the voltage relation profile for weakly and highly charged states (arrows in Fig.2d) shows two different time of equilibrium. The voltage of the highly charged state (top insert in Fig.2d) did not fully relax even for rest period close to one day, hence indicating a process with a large time constant. This contrasts with the small time constant observed for the low voltage charge state (bottom insert in Fig.2d) and equally for various discharge voltage states.

The origin of such a difference was explored experimentally through *operando* XRD on $NaLi_{1/3}Mn_{2/3}O_2$/Na half cell. The cell was cycled at a C/20 rate and XRD patterns were collected for every change in sodium stoichiometry of 0.05 (Supplementary Fig. 13). Our data reveal several electrochemically driven biphasic and solid solution regions. Initially, a biphasic process is observed with the appearance of a new phase O3 (II) having an increased *c* lattice parameter (~5.64 Å) compared to the pristine O3 (I) phase (~5.58 Å). Further pursuing the desodiation leads to a narrow solid solution through which the *c* lattice parameter initially contracts prior to decrease rapidly, once the O_2 evolution potential is reached, leading to the O3(III) phase at the very end of charge. An in-depth exploration of the crystal structure evolution in different states of charge and discharge was undertaken using synchrotron XRD (Fig. 3). Rietveld refinements (Supplementary Table 4−5) show that all patterns (middle, end of charge and discharge) can be indexed with O3 ($R\bar{3}m$) structures that solely differ in lattice parameters while containing copious amount of micro-strain. Note that we did not use the

*C*2/*m* space group to refine the patterns, because the $[Li_{1/3}Mn_{2/3}]O_2$ honeycomb superstructure reflections are barely visible and no splitting resulting from a monoclinic distortion is observed. We therefore conclude that the O3-P3 phase transition, very frequently reported upon removal of Na^+ in O3 sodium layered oxide is not observed with $NaLi_{1/3}Mn_{2/3}O_2$. This suggests the absence of Na-vacancy ordering in $Na_{1-x}Li_{1/3}Mn_{2/3}O_2$ that is usually proposed as the origin of the O3-P3 phase transition[22] in Na-based layered oxides.

Turning to oxygen deficiency, two models with and without oxygen vacancies (as deduced by OEMS) were tried for the fully charged $Na_{0.09}Li_{1/3}Mn_{2/3}O_2$ sample but both giving refinements of comparable quality preventing reliable assignment (Supplementary Fig.14). In contrast, models having Mn placed in either octahedral or tetrahedral sites within the Na interlayer spaces deteriorate the refinement with respect to the one having Mn solely located in the transition metal layers (Supplementary Fig.15), hence suggesting the absence of manganese migration to the alkali layer. This was confirmed by refining the NPD pattern collected for the fully charged sample of which the best fit was obtained with Mn in the metal layers together with all the Li and remaining Na atoms being in the alkali layers so that the resulting chemical formula can be written as $[Na_{0.09}Li_{1/3}]_{interlayer}[(\square_{cat})_{1/3}Mn_{2/3}]_{metal}O_{1.86}$ (Fig.3d, Supplementary Table 6). Lastly, it is of paramount importance to note, that the peaks in SXRD corresponding to the honeycomb superstructure largely reduce in intensity through the first charge and discharge processes. Such disappearance of superstructure peaks can be either associated with the collapse of the honeycomb ordering due to metal ion migration within the metal layers or with an increased amount of stacking faults that reduce the long range ordering.

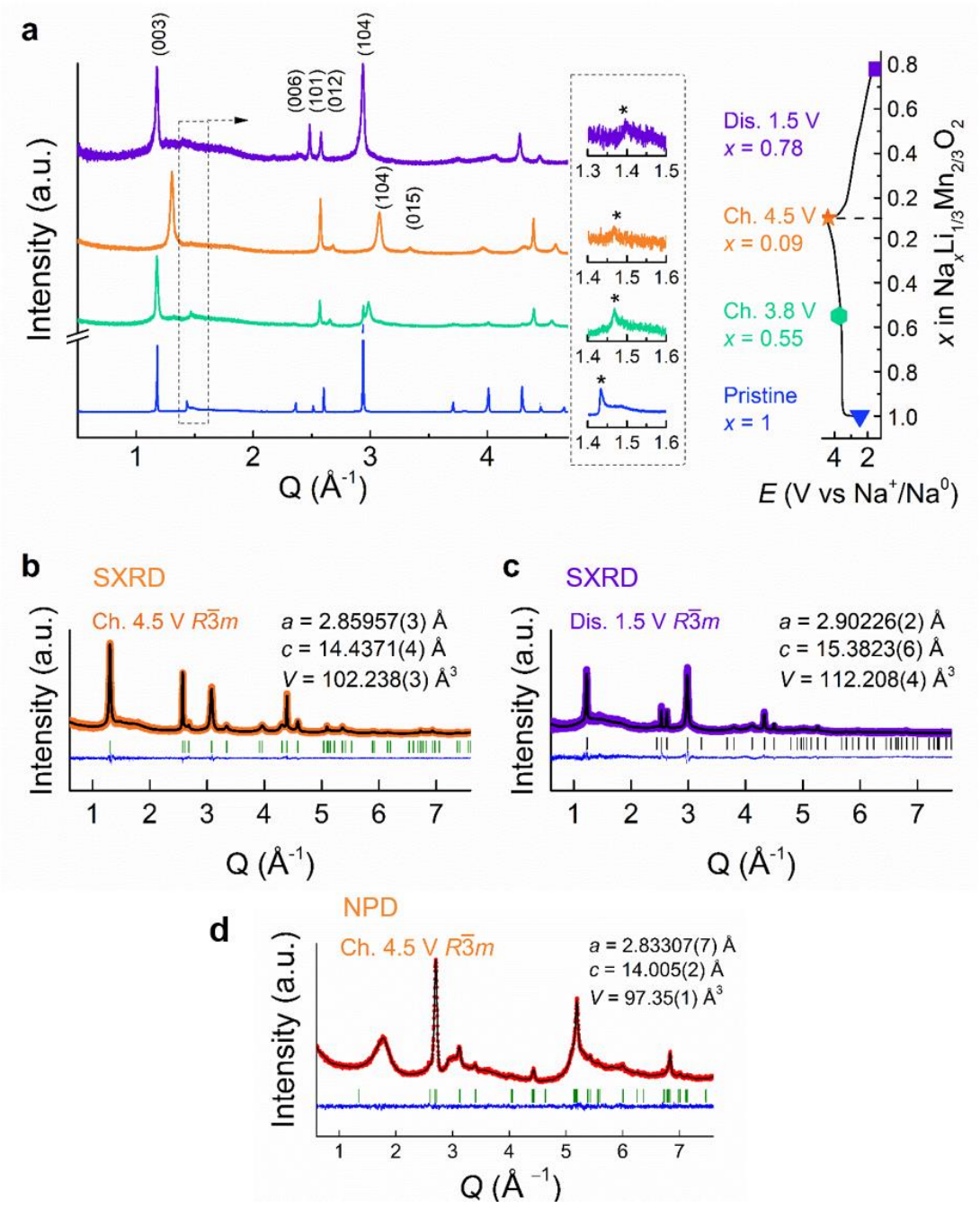

Fig. 3 Structural evolution in the first cycle. a, (left) SXRD patterns of pristine (blue), *ex situ* samples stopped at mid-charge (green), end of charge (orange) and end of discharge (purple) of the initial cycle. Zoomed view of superstructure peaks (marked by asterisks) together with the *ex situ* points on the electrochemistry curve are illustrated on the right. **b**, **c**, Rietveld refinement of the SXRD patterns of the fully charged and fully discharged samples, respectively. All the SXRD were indexed in $R\bar{3}m$ space group (O3 structure) having the lattice parameters, a = 2.92441(1) Å, c = 15.96473(9) Å, V = 118.241(1) Å^3 for pristine; a = 2.86135(6) Å, c = 16.067(1) Å, V = 113.922(9) Å^3 as the major phase for the mid-charged $Na_{0.45}Li_{1/3}Mn_{2/3}O_2$; a =2.85957(3) Å, c = 14.4371(4) Å, V = 102.238(3) Å^3 for the fully charged $Na_{0.09}Li_{1/3}Mn_{2/3}O_{1.86}$; and a =2.90226(2) Å, c = 15.3823(6) Å, V =112.208(4) Å^3 for the fully discharged $Na_{0.78}Li_{1/3}Mn_{2/3}O_{1.86}$. **d**, Rietveld refinement of the NPD pattern of the fully charged sample in $R\bar{3}m$ space group (O3 structure) with a = 2.83307(7) Å and c = 14.005(2) Å, V =97.35(1) Å^3. The oxygen content was fixed to 1.86 per formula unit, and different structural models were tested that differ in the Mn, Li and Na distribution in the metal layer and/or

interlayer sites. The best fit was obtained with Mn in the metal layers, and interlayers accommodating all Li atoms and remaining Na, so that the resulting chemical formula can be written as $[Li_{1/3}Na_{0.09}]_{interlayer}[(\square_{cat})_{1/3}Mn_{2/3}]_{metal}O_{1.86}$ (see Supplementary Table 6 for more details).

High angle annular dark field scanning transmission electron microscopy (HAADF-STEM) was next used to grasp further insights into local structure of $NaLi_{1/3}Mn_{2/3}O_2$ upon Na^+ removal and uptake. Our data confirms the presence of O3-type layered structure for the pristine sample that is maintained in the samples charged to 4.5 V and discharged to 1.5 V, as evidenced by the [010] SAED patterns in Fig. 4. The [010] HAADF-STEM images also confirm the O3-type stacking demonstrating the lateral displacement of the $[Li_{1/3}Mn_{2/3}]O_2$ layers by 1/3 of the distance between two neighboring dots denoting the Mn columns (Fig. 4). No additional intensity was observed between the $[Li_{1/3}Mn_{2/3}]O_2$ layers in the HAADF intensity profiles (except of very faint dots of the Na columns barely visible at the thicker part of the pristine $NaLi_{1/3}Mn_{2/3}O_2$ crystallite (Fig. 4a, left)) that agrees well with the absence of Mn migration to the Na sites in the charged 4.5 V and discharged to 1.5 V states, as deduced from SXRD. After charge and discharge for 10 cycles, the O3 structure remained (Supplementary Fig.16). The reflections in the SAED patterns are very broad and streaked with diffuse intensity along the ***c**** axis, which is not surprising given the enormous anisotropic broadening observed from SXRD (Supplementary Fig.17). HAADF-STEM images show that the reflection broadening and diffuse intensity originate from pronounced local structure distortions, where the $[Li_{1/3}Mn_{2/3}]O_2$ layers become wavy, demonstrating strong local variations of the interlayer distance. The HAADF-STEM images of the sample after 10 cycles show that Mn migration to the interlayer space occurs only at the top surface areas, and not in the more bulky parts. Another feature is the significant suppression of the honeycomb ordering visible in both SAED pattern and the HAADF-STEM image (Supplementary Fig.16). Overall, combined SXRD and TEM results unambiguously confirm the absence of out-of-plane Mn migration in $NaLi_{1/3}Mn_{2/3}O_2$ with therefore signs of in-plane migration increasing with cycling.

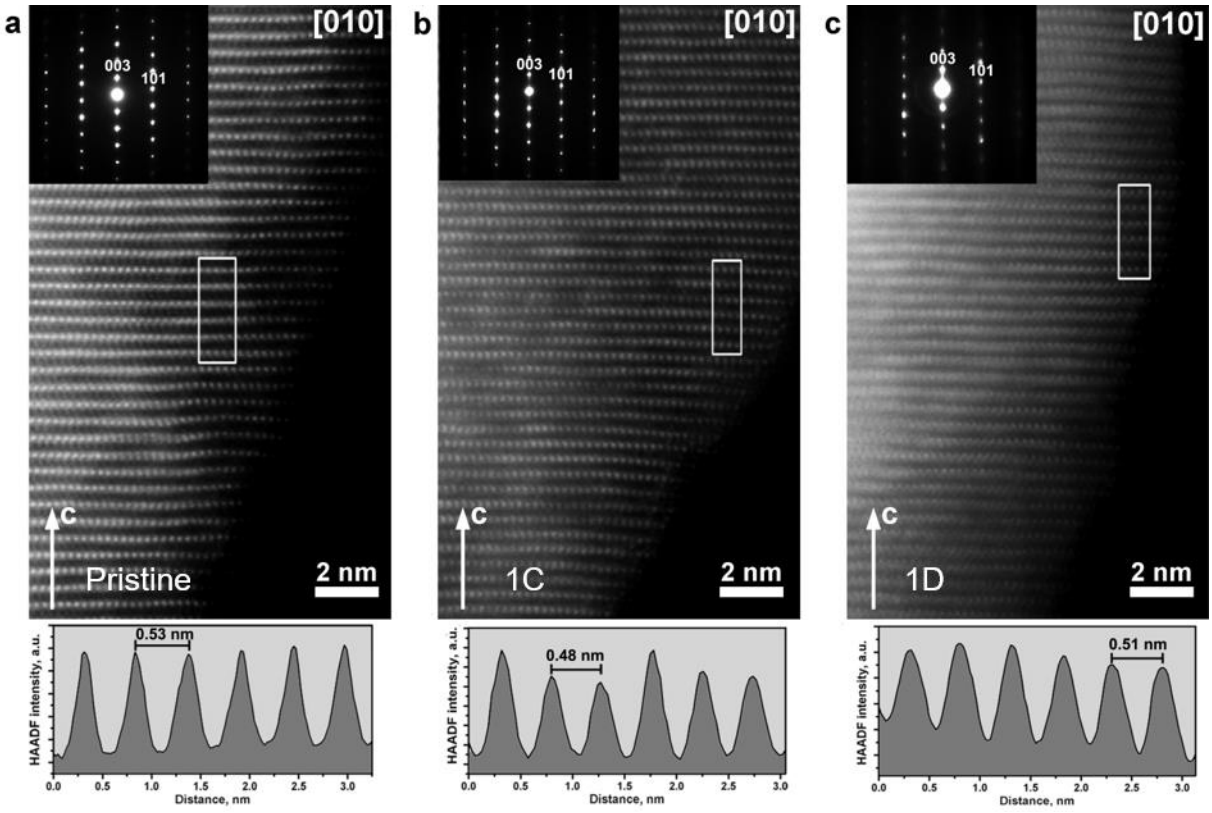

Fig. 4. **Structural analysis by microscopy.** [010] HAADF-STEM images and corresponding HAADF intensity profiles across the $[Li_{1/3}Mn_{2/3}]O_2$ layers in the outlined rectangular areas for (a) pristine, (b) charged to 4.5 V and (c) discharged to 1.5 V $NaLi_{1/3}Mn_{2/3}O_2$. Corresponding [010] SAED patterns are given in the insets; the patterns are indexed as the O3 $R\bar{3}m$ phase. The peaks in the HAADF intensity profiles correspond to the Mn columns solely at the $[Li_{1/3}Mn_{2/3}]O_2$ layers, whereas absence of the intensity between the peaks indicates no Mn migration into the Na layers.

In absence of Li^+ loss from the structure, as deduced from ICP-OES, a legitimate question regards its structural role through the Na (de)insertion process. To evaluate its impact, both ^6Li and ^{23}Na Nuclear Magnetic Resonance (NMR) spectra were recorded on $Na_{1-x}Li_{1/3}Mn_{2/3}O_2$ at various states of charge and discharge (Fig. 5). Both ^6Li (Fig.5C) and ^{23}Na (Fig.5D) spectra show two signals for the pristine material with in each case a nearly 1 to 2 balance. The doublet for Na is consistent with the *C*2/*m* structure having two different sites (2*c* and 4*h*) for Na^+ (Fig. 5B). The large shift to ~1400 ppm in the ^6Li Lorentzian line is indicative of the presence of lithium in transition metal $[Li_{1/3}Mn_{2/3}]O_2$ layer[33]. Moreover, the two slightly different environments causing two lines at 1400 and 1450 ppm most likely arise from the difference in Li position due to the frequent violation of periodicity along the stacking direction of the honeycomb TM layers (see Fig.1b, Supplementary Fig.7). Upon charging, this signal (blue) progressively disappears to the expense of a new one (green) with a significantly different chemical shift centered around ~700 ppm that becomes unique for the fully charged sample. In light of previous studies, this new signal is assigned to Li^+ ions

sitting in octahedral coordination within the alkali metal layers,[34,35] in full agreement with the NPD data (Fig.3d, Supplementary Table 6). An additional feature is the partial irreversibility of this Li-site migration upon discharge since the peak at 700 ppm remains large (75% of the total) for the fully discharged sample (spectrum g in Fig. 5C). The irreversible migration of lithium is likely responsible for the wavy nature of the $[Li_{1/3}Mn_{2/3}]O_2$ layers and the strong local variations of the interlayer distances observed by HAADF-STEM. Lastly, the integration of the ^{6}Li signal through the process remains constant further confirming that no Li is lost (as seen from ICP-OES measurements in Supplementary Fig. 8) and all ^{6}Li spins are detected by NMR. This is in contrast to previous studies, where a similar behavior of lithium was observed but lithium loss could not be prevented.[36,37]

The ^{23}Na NMR spectra upon charging first show the progressive disappearance of the 1980 ppm shift (yellow) to the benefit of the 2170 ppm one (grey) implying that the Na^+ ions are initially removed from the 4*h* position. This signal becomes unique, showing an almost single Na environment after removal of 0.55 Na^+ corresponding to the 2*c* positions (spectrum c in Fig. 5D), indicative of a reorganization of Na sub-lattice associated to the early Li displacement. Afterwards, there is a dramatic change in the sodium environment and the signal is now shifted to lower chemical shifts (1300 ppm) and much broadened (800 ppm vs 250-500 ppm), signifying an increase in the local disorder around the remaining sodium ions, which amount to nearly ~ 0.09 Na per formula unit in the fully charged sample. The origin of such disorder is most likely linked to the onset of O_2 release, which starts between points c and d in Fig.5A according to the OEMS measurement. Moreover, the existence of a very broad peak is also compatible with the slow Na^+ dynamics which prevents the averaging of the shift, and may explain the hysteresis observed in GITT measurements at high potential. Upon discharge, the initial signals are not recovered since the reinsertion of Na^+ leads to a very broad (> 1300 ppm) Gaussian distribution of environments, indicative of the persistence of a massive structural disorder resulting from a broader distribution of Na-O-Mn angles which govern the NMR shifts[37]. Note that the ^{23}Na NMR spectrum for a subsequently recharged sample (Supplementary Fig.18) shows a broad line, centered at a lower shift of 910 ppm, but with a width of 650 ppm that is solely half as wide as at the end of the first charge, indicating that, somehow, some local order is restored during the second cycle.

Consistently, similar broad ^{23}Na NMR signals were previously reported for the fully $Na_xNi_{0.5}Mn_{0.5}O_2$ phase with disordered Na occupation.[38] Thus, this scenario could in fact explain the difference in cycling curve between first charge-discharge and also the absence

O3 to P3 phase transition (*operando* XRD in Supplementary Fig.13) since the irreversibly migrated lithium may arrest the long range zig-zag ordering of Na and vacancy which is required to stabilize the P3 phase[22].

Altogether, NMR results show that upon Na^+ removal, $Na_{1-x}Li_{1/3}Mn_{2/3}O_2$ undergoes a partially irreversible migration of Li^+ to the Na layers that creates cation vacancies and disorder within the $[Li_{1/3}Mn_{2/3}]O_2$ layers. Due to such an intense modification of the structure, some of the Na^+ cannot any longer fully return to their initial sites as some of them are irreversibly occupied by 0.25 lithium ions per unit formula (explaining the irreversible loss of 0.23 Na during the first charge/discharge cycle). Therefore, they will occupy sites having changed coordination, explaining the broadened spectra.

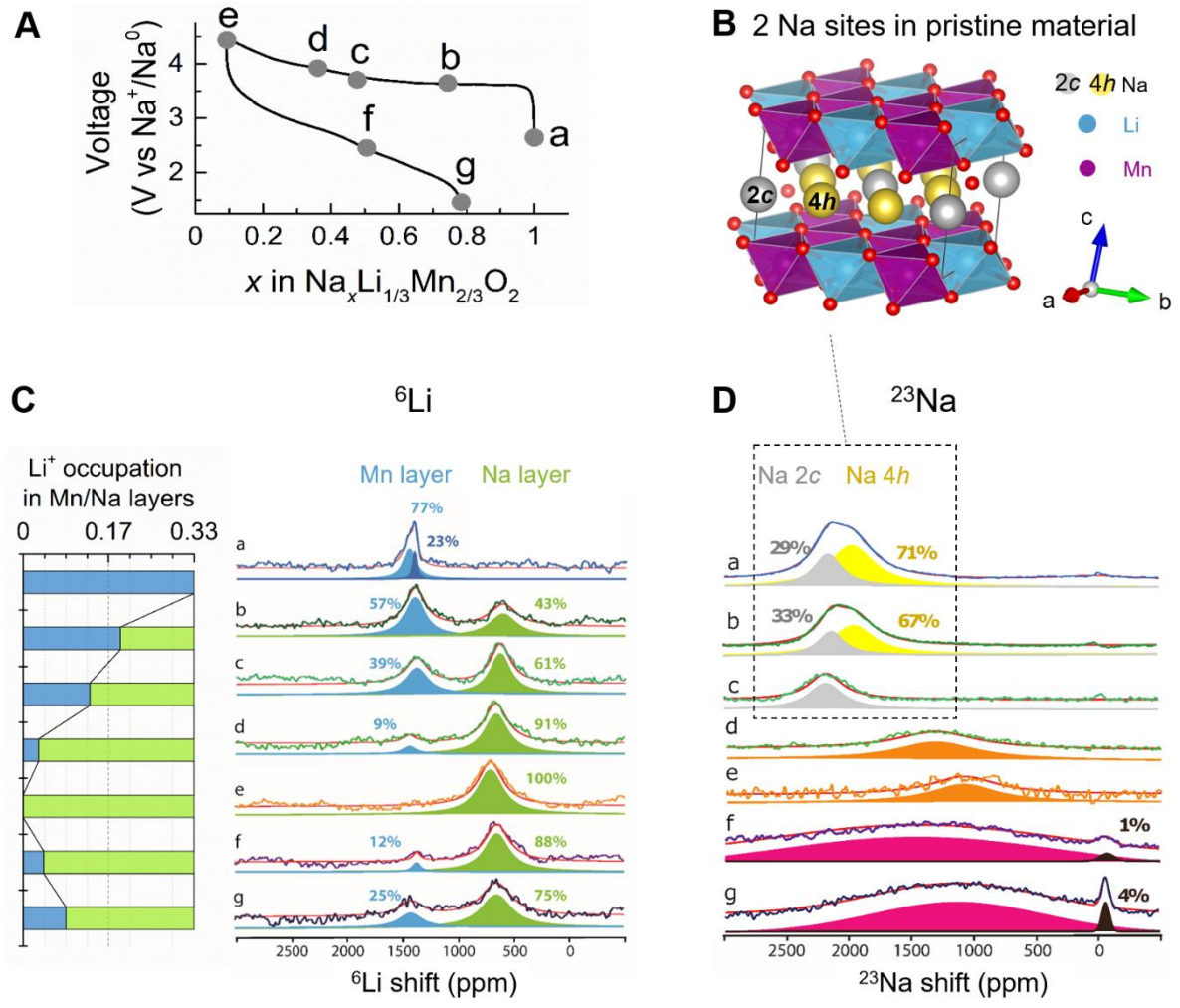

Fig. 5 ^{6}Li and ^{23}Na MAS NMR spectroscopy results. A, First-cycle charge-discharge voltage profile with points indicating states of charge/ discharge at which the *ex situ* samples were extracted. **B**, Crystal structure of the pristine $NaLi_{1/3}Mn_{2/3}O_2$ (space group *C*2/*m*) showing two Wyckoff sites (2*c* and 4*h*) for Na^+. **C**, ^{6}Li MAS NMR spectra showing two types of peaks corresponding to the isotropic shifts for Li in the $[Li_{1/3}Mn_{2/3}]O_2$ layers (blue) and alkali layers (green). Li^+ population in both

environments are compared in stacked bar chart on the left as guide to the eye. **D**, ^{23}Na MAS NMR results showing peak shifts and broadening. The two Na^+ signals in the pristine material can be understood by the two distinct crystal sites shown in figure panel B (see text). The two sharp peaks at nearly 0 ppm in f and g are due to trace amounts of remaining Na salt from the electrolyte that left unwashed.

Next we interrogate the nature of the electrochemically driven redox processes and their interplay with local structural changes in $Na_{1-x}Li_{1/3}Mn_{2/3}O_2$. Complementary *operando* X-ray Absorption (XAS), *ex situ* Hard X-ray Photoelectron Spectroscopy (HAXPES) and mapping of Resonant Inelastic X-ray Scattering (mRIXS) were used to probe the sample at various depths (particles are of > 0.5 μm size as seen by SEM, Supplementary Fig. 19). During the first charge (Fig. 6, a–c) all the techniques show features related solely to oxygen oxidation. The O1*s* HAXPES spectra (Fig. 6a, Supplementary Fig. 20, 21, left) of the pristine and fully charged samples differ by the appearance of a new peak at binding energy (*BE*) of 530.5 eV for the fully oxidized sample that corresponds, in light of previous reports,[39] to oxidized lattice oxygen O^{n-} ($n < 2$). This oxygen activity is unambiguously confirmed by the appearance of a new feature in mRIXS (outlined by an ellipse in Fig. 6b), at an excitation and emission energy of 531.0 eV and 523.7 eV, respectively, that is characteristic of O^{n-} species.[40] This feature disappears and reappears on subsequent charge-discharge confirming the reversibility of the anionic redox process (Supplementary Fig. 22). Turning to the outcome of Mn^{4+} during the first oxidation process, Mn2*p* HAXPES (Supplementary Fig. 20, 21, right), Mn L_3 mRIXS (Supplementary Fig. 23, 24), *ex situ* and *operando* XAS on Mn K edge (Supplementary Fig. 25, 26) indicate that Mn^{4+} is redox inactive on first charge since there is no evolution in the Mn oxidation state in neither of the techniques between pristine and fully charged sample.

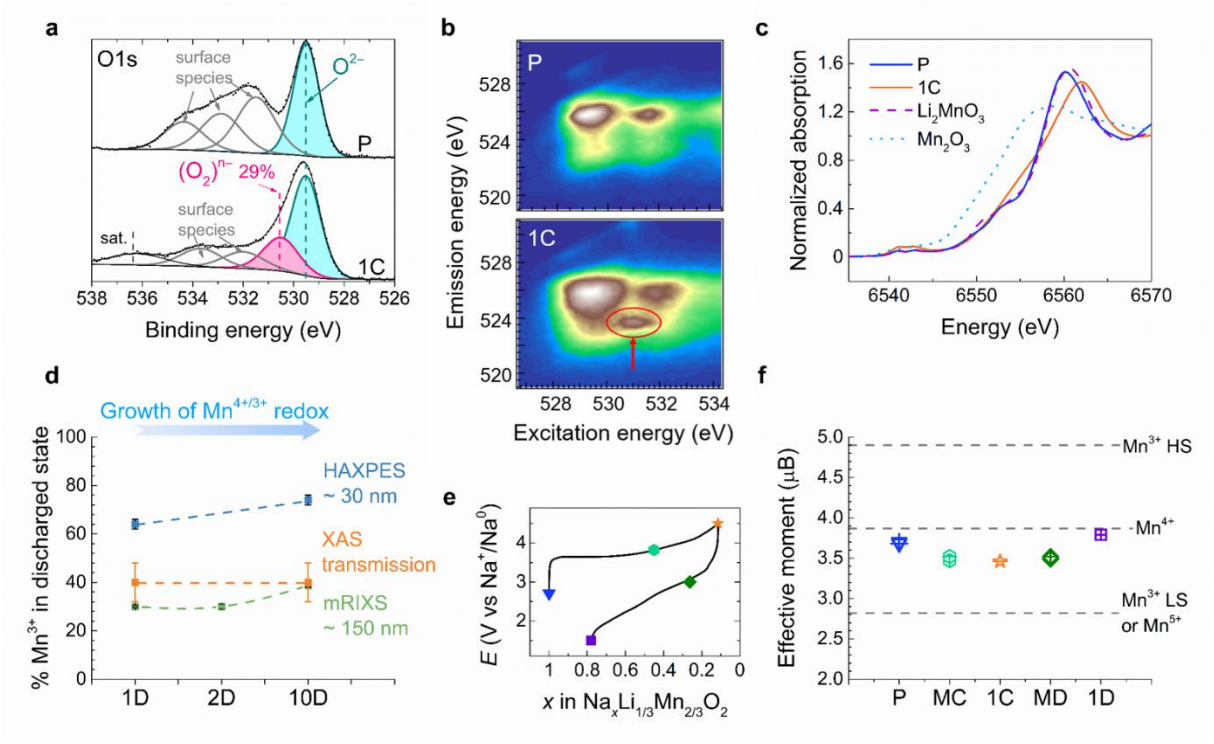

Fig.6 Charge compensation mechanism in $NaLi_{1/3}Mn_{2/3}O_2$. a, *ex situ* HAXPES ($h\upsilon$ = 6900 eV) O1*s* spectra of pristine (P) and charged to 4.5 V samples (1C). **b**, *ex situ* O K-edge mRIXS spectra of pristine (P) and sample charged to 4.5 V (1C). Red arrows and circles at 531.0 eV excitation energy and 523.7 eV emission energy indicate the oxidized oxygen feature at charged state. **c**, Mn K-edge XANES spectra of pristine (blue solid) and sample charged to 4.5 V (orange solid), compared to references of Mn^{4+} (purple dashed) and Mn^{3+} (cyan dotted). **d**, Concentration of Mn^{3+} species derived from *ex situ* HAXPES, mRIXS and XAS in the 1st, 2nd, and 10th discharged 1.5 V samples. **e**, First cycle charge-discharge curve with points indicating the state of charge/ discharge at which *ex situ* samples for magnetic measurements were extracted from. **f**, Effective magnetic moment deduced from magnetic susceptibility measurements. P, MC, 1C, MD and 1D represents pristine, mid-charge, first charge, mid-discharge and first discharge samples, respectively. Dashed lines indicate theoretical values of spin-only effective magnetic moments of Mn at different oxidation states and spin states.

On discharge, all the techniques converge in showing conjointly a nearly reversible oxygen redox process together with a varying degree of reduction from Mn^{4+} to Mn^{3+} (Supplementary Fig. 20−26). However, they show discrepancies in quantifying the amount of Mn^{3+} (Fig. 6d). For instance, HAXPES, which is mainly a surface technique (~30 nm in depth), indicates nearly 60% of Mn^{3+} in the fully discharged sample as opposed to solely ~30 % with mRIXS, which has a probe depth of ~150 nm, compared to a total thickness of the cathode of ~40 μm.

A comprehensive view of the electrode ensemble can be acquired from XAS measurements at the Mn K-edge, which was collected in transmission geometry. Despite the clear trend of Mn reduction as the edge shift to lower energies in discharge (Supplementary Fig. 25, 26), quantification via linear combination fits of references, as performed for Mn L_3

mRIXS, was not possible because the position and shape of the Mn spectra at K-edge heavily depend on both formal oxidation state and coordination environment of Mn.[41] To account for variations in line shape introduced by changes in coordination environment, the spectra were analyzed following the integration method proposed by Dau et al.[42] Such approach rendered an approximate average oxidation state of ~3.6+ for the discharged (1D) sample (Supplementary Fig. 25b), consistent with the quantification from Mn L_3 mRIXS (Supplementary Fig. 24, Figure 6d). It is worth noting that we found the linear fit in this method is still rather sensitive to the choice of reference spectra, leading to a larger uncertainty than with other methods. The difference between HAXPES and the mRIXS and XAS results could be ascribed to differentiated surface reactivity worth exploring in future work, but, in all, it is clear that partial reduction of Mn^{4+} into Mn^{3+} occurred during the first discharge, reminiscent to the behavior of the parent Li_2MnO_3.[43] However, the degree of Mn reduction was lower than expected from the measured capacities, pointing to complex charge compensation. Lastly, independent of the spectroscopy employed, the changes in Mn spectra were reproduced upon extensive cycling, proving that Mn redox couple was activated after the first charge (Supplementary Fig. 21, 24, 25).

Alternatively, *ex situ* magnetic susceptibility measurements from 2 to 400 K carried out on the samples at various states of charge and discharge (Fig. 6e) (Supplementary Fig. 27, Supplementary Table 7) confirm the presence of Mn^{4+} with a magnetic moment close to the expected value in the pristine material (μ_{eff} ~3.7 μB vs. 3.9, Fig6f) and displaying a valley-like variation upon cycling Such a mirror variation in charge/charge is surprising considering that the partial reduction of $Mn^{4+} \rightarrow Mn^{3+}$ should lead to an increase of μ_{eff}. Given the significant amount of Mn3+ determined by spectroscopy, the small increase of μ_{eff} in the discharge sample compared to the pristine one (3.79 vs. 3.7 $\mu_{B,}$) strongly suggests charge transfer between Mn and O during oxidation. This indirectly supports the participation of anions in the redox activity of $NaLi_{1/3}Mn_{2/3}O_2$, as corroborated by our recent theoretical calculations on $Na_{2/3}[Mg_{1/3}Mn_{2/3}]_2$[44] showing that the coupling unpaired electrons on both Mn and O the decreases the total magnetization of the cell. However, it is beyond the scope of this paper to quantitatively decouple the Mn from the O contribution for μ_{eff} values, whose robustness is ensured by having duplicated twice our measurements on different samples.

Overall, we report a novel anionic redox active O3 $NaLi_{1/3}Mn_{2/3}O_2$ layered phase vs. Na showing no voltage fade and oxygen redox not associated with 3*d* metal migration to the alkali layer, unlike most Li-rich layered oxides. Moreover, it turns out that $NaLi_{1/3}Mn_{2/3}O_2$ is

an ideal model compound to clarify the key role of the alkali metal in Li(Na)-rich layered oxides with respect to both voltage fade and 3*d* cation migration owing to its versatility to intercalate Na and Li as shown next. A nearly Na-free electrode, $Na_{0.09}Li_{1/3}Mn_{2/3}O_{1.86,}$ was recovered and washed from a $NaLi_{1/3}Mn_{2/3}O_2$/Na Swagelok cell that was fully charged to 4.5 V, prior to be used in a new Swagelok with Li metal as a negative electrode and 1M $LiPF_6$ in EC-DMC (v/v = 50/50, LP30) as electrolyte. The voltage profile for the $Na_{0.09}Li_{1/3}Mn_{2/3}O_2$/Li cell (Fig. 7a) shows the reversible uptake of 0.4 Li^+ per formula unit together with good capacity retention upon cycling, yet accompanied by large voltage decay. From combined coulombic titration and ICP analysis, the chemical composition of the fully discharged sample was identified as $Na_{0.09}Li_{0.73}Mn_{2/3}O_2$.

Evidence for Mn migration upon Li insertion in this material was obtained by TEM. The [010] HAADF-STEM images and corresponding HAADF intensity profiles across the $[Li_{1/3}Mn_{2/3}]O_2$ layers are reported after one (Fig. 7c) and ten (Fig. 7d) charge-discharge cycles in Li-ion half cells. The outlined rectangular areas reveal the Mn cation migrations that are enhanced with cycling. The peaks in the HAADF intensity profiles (bottom) correspond to the Mn columns at the $[Li_{1/3}Mn_{2/3}]O_2$ layers, whereas the intensity between the peaks (marked with black arrowheads) indicates the migration of the Mn cations into the interlayer space. Note that the Mn migration is more pronounced in the sample after 10 cycles which indicates only partially irreversible character of this migration. This drastically contrasts with similar images taken on the material cycled vs. Na in Na-based electrolytes where no Mn migration towards the alkali layer can be spotted.

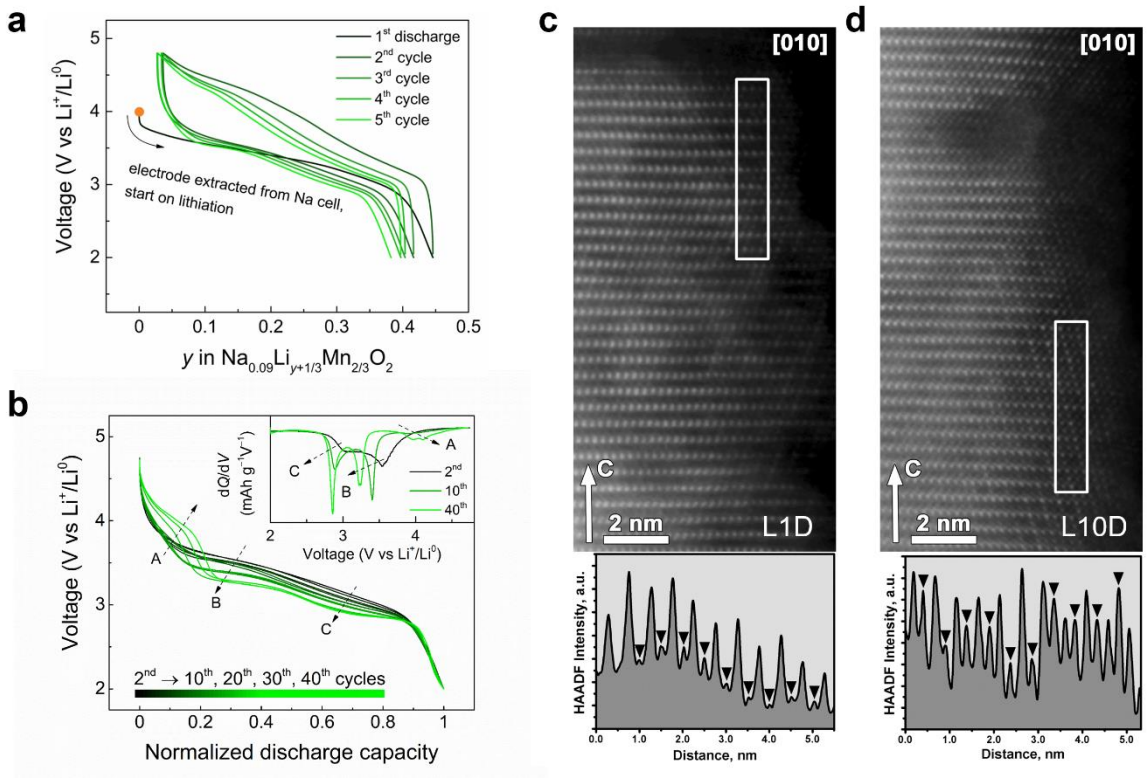

Fig. 7 Voltage fade and cation migration in Li half cells. a, First five cycles of voltage-composition profiles of the desodiated $Na_{0.09}Li_{1/3}Mn_{2/3}O_{1.86}$ cycled in Li half cells with LP30 electrolyte. **b**, normalized discharge curves of the same cell for 40 cycles with d*Q*/d*V* of selected cycles, showing the evolution of low voltage redox process and voltage fade upon cycling in the Li cell. The actual discharge profile before normalization is given in Supplementary Fig. 28. [010] HAADF-STEM images and corresponding HAADF intensity profiles show increasing cation migration from the **c**, 1st discharged to **d**, 10th discharged sample in the Li cell.

Discussion

Altogether, the electrochemical activity of Na (Li) in the alkali-rich $NaLi_{1/3}Mn_{2/3}O_2$ phase provides valuable information for clarifying the complex interplay between anionic redox, cationic migration, voltage hysteresis and voltage fade in layered 3*d* transition metal oxides. It now pertains to confront these findings with existing literature data to move one-step forward in the general understanding of the anionic redox mechanism.

Among the Na-based anionic redox active layered compounds so far reported, O3-$NaLi_{1/3}Mn_{2/3}O_2$ is the one that shows the lowest oxygen redox potential (~3.6 V vs Na^+/Na). To rationalize this finding DFT calculations were performed on the *C*2/*m* structural model of multiple variations of partially charged O3-$Na_xLi_{1/3}Mn_{2/3}O_2$ structures with the Li^+/Na^+ cations distributed over three crystallographic positions 2*b* (Mn layer) and 4*h*, 2*c* (alkali layer). Up to the removal of 1/3 Na^+, all O3 configurations with partial or total Li migration to the alkali layer, namely Li(M+A) or Li(A) are significantly destabilized against those having Li

in the Mn layer, namely Li(M). This energy penalty for Li migration to the alkali layer is removed upon further Na^+ extraction as Li(M+A) and Li(A) configurations become as stable or more stable than Li(M) configurations at Na concentration x_{Na} = 1/3 and 1/6, respectively. (Supplementary Table 8). Remarkably, the Mn^{4+} (0.54 Å) migration to the alkali layer is energetically prevented due to a significant destabilization of the MnO_6 octahedron that would display much too long Mn-O bonds when sitting in the alkali layer (2.2 Å) compared to the metallic layer (1.9 Å). This thermodynamic preference for Li migration is likely related to the well-known interlayer electrostatic instability of layered oxides at low alkali-content and is here activated once the Na/Li concentration ratio reaches 1 in $Na_x(Li_{1/3}Mn_{2/3})O_2$. This ratio therefore sets the critical Na concentration below which Li rather than Na should dominate the crystallographic features of the O3 phase. Accordingly, Li migration at $x_{Na} \leq 1/3$ comes along with a significant contraction of the *c* lattice parameter, which obviously affects the kinetics of Na^+ diffusion for further de-sodiation. Altogether, these results allow reconciling the XRD, NMR and electrochemical data and help in rationalizing the role of Na on the stabilization of the O3 phase.

Upon Na removal, a biphasic process occurs between x_{Na} = 1 and x_{Na} ~2/3 for which the computed average potential (3.5 V) is in fair agreement with experiments (Supplementary Table 8). The end-member $Na_{2/3}[Li_{1/3}Mn_{2/3}]O_2$ phase of this biphasic process displays an increased *c* lattice parameter compared to the pristine phase, fully consistent with the O3(II) phase identified by *operando* XRD (Supplementary Fig.13) at the very beginning of charge. Removing more sodium from the structure leads to $Na_{1/3}[Li_{1/3}Mn_{2/3}]O_2$ or $Na_{1/6}[Li_{1/3}Mn_{2/3}]O_2$ phases having Li in the alkali layer and contracted *c* lattice parameters, consistent with the less chemically shifted ^{6}Li NMR signal observed in Fig.5C and the crystallographic features of O3(II) just before the onset of O_2 release (Supplementary Table 8). Interestingly, further Na^+ removal from the Li-migrated O3(II) phase (Supplementary Fig.13) should be kinetically hindered by the size-constrained alkali interlayer, hence leading to the voltage polarization observed in the galvanostatic curve of Fig.2 along the second process. We believe this kinetic limitation of Na-ion diffusion in the structure most likely prevents the Na-ordering required for the O3 to P3 transition. Moreover, it is at this stage of the Na removal process, when nearly all Li has moved to the alkali layers (as deduced from ^{6}Li NMR) that O_2 release is triggered. This observation is not fortuitous since Li migration to the alkali layer implies that some oxygen atoms become less electrostatically bonded to the structural network due to cationic vacancies in their local environment and therefore more prone to oxidation.

Noteworthy, the presence of Li vacancies in the metallic layer may also favor Mn/Li_{vac} disorder in the metallic layer, as observed in the synchrotron XRD and TEM data. While no evidence of ribbon ordering[14] was found in the XRD patterns of the charged sample, the Mn/Li_{vac} disorder is predicted to be thermodynamically achievable at low Na content (x_{Na} = 1/6) which should prevent Li^+ ions from moving back to the metallic layer in discharge (Supplementary Table 9). Obviously, towards the very end of charge (x_{Na} < 1/6), the phases determined by DFT calculations without considering O_2 release may no longer be representative of the experimental ones. Therefore, a thorough analysis of O-defective phases that enlists, besides O- and Na-vacancies, the migration of Mn within the metallic layer, would be required to get more insights into the impact of these structural modifications on further cycling.

Another intriguing question regards whether the O_2 release leads to oxygen vacancies or material densification, which has so far been associated solely to the migration of the transition metal cations into the alkali metal layers in the Li-rich layered oxides. In $NaLi_{1/3}Mn_{2/3}O_2$ such interlayer migration can safely be excluded based on the XRD and TEM structure analysis. First-principles DFT calculations confirm this point by showing that Mn migration from the metallic to the alkali layer is thermodynamically less favored (by at least 200-300 meV/Mn, Supplementary Table 9) when the alkali layer contains Na compared to Li, even at low sodium content. This suggests that the presence of Na^+ ions in the alkali layer, even in small amount, imposes much too large interlayer spacing (large *c* parameter) to stabilize Mn^{4+} in the octahedral site. Moreover, we could also compute with DFT the variation of the *c* parameter from the fully sodiated $Na[Li_{1/3}Mn_{2/3}]O_2$ phase to the desodiated $Na_{0.125}[Li_{1/3}Mn_{2/3}]O_2$ one which nicely follows the experimental data reported from XRD analysis in Fig.3a only when Li migration is considered in the partially desodiated $Na_{1/3}[Li_{1/3}Mn_{2/3}]O_2$ phase (Supplementary Table 8). In contrast, the *c*-parameter for pure-Li phases is systematically smaller by at least 1.5 Å, which again confirms the greater ability of Li-based phases to stabilize the Mn cations in the interlayer space. Interestingly, O3-$Na_{0.09}Li_{1/3}Mn_{2/3}O_2$ on Li-insertion behaves similarly to the pure Li-phases, as Li^+ occupies positions in both alkali and metallic layers.

Consequently, we could hastily eliminate the densification hypothesis prior to realizing that Mn migration within the metal layers could be an alternative way to trigger densification. The complete migration of Li^+ cations from the $[Li_{1/3}Mn_{2/3}]O_2$ layer to the alkali layer on the first charge leaves cationic vacancies ($\square_{cat}$), and, taking into account oxygen release at high voltage,

the chemical formula for the fully charged state can be represented as $Na_{0.09}Li_{1/3}[(\square_{cat})_{1/3}Mn_{2/3}]O_{1.86}$ Realization of oxygen deficiency through anion vacancies should lower the coordination number of Mn below six, but Mn K-edge XANES spectra and EXAFS reveal octahedral Mn coordination at all states of charge. Thus the oxygen vacancies must be eliminated by migration from bulk to the surface with subsequent annihilation and the increasing Mn/O ratio is accommodated by intralayer Mn^{4+} cation migration to vacant cation sites $\square_{cat}$. The chemical formula at full charge can be recast as $Na_{0.09}Li_{0.36}[(\square_{cat})_{0.28}Mn_{0.72}]O_2$. Disrupting the 1:2 ($\square_{cat}$):Mn ratio should suppress the honeycomb cation ordering and promote stochastic arrangement of Mn^{4+} and cation vacancies in the densified $[(\square_{cat})_{0.28}Mn_{0.72}]O_2$ layers, as indicated by vanishing intensity of the honeycomb superlattice reflections in the SXRD patterns (Fig. 3a) and confirmed by DFT calculations (Supplementary Table 9)

Our study also showed that discharging of the O3-$Na_{0.09}Li_{1/3}Mn_{2/3}O_{1.86}$ material either in Na-ion or in Li-ion cells promote intralayer and interlayer cation migration, respectively, therefore comforting the robustness of the interplay between cationic migration and voltage fade early proposed.[45] The O3-$NaLi_{1/3}Mn_{2/3}O_2$ phase exemplifies very clearly that if the densification after first oxygen release occurs through the intralayer transition metal cation migration, the material demonstrates virtually no voltage fade, whereas switching to the interlayer migration mode (e.g., cycling vs. Li^+/Li^0) readily introduces voltage fade. Therefore, a new way to mitigate voltage fade could consist in promoting the intralayer migration of transition metal by controlling, via chemical composition, the structural location of vacancies formed by alkali cation de-insertion with respect to the onset of oxygen release. The benefit associated to the absence of voltage fade for O3-$NaLi_{1/3}Mn_{2/3}O_2$ is however tarnished by the fact that the Na uptake-removal in this phase comes with a large voltage hysteresis. Numerous explanations enlisting either reformation/breaking of O-O dimers[46], cationic-anionic redox inversion induced by small charge-transfer bandgap[47] or sluggish structural rearrangements[48] have so far been proposed to account for such hysteresis with the most favored one being interlayer transition metal migration during the first oxidation.[49–51] We could hypothesize that the hysteresis observed in O3-$NaLi_{1/3}Mn_{2/3}O_2$ is also due to intralayer Mn migration, but further in depth investigation is needed. If true, the voltage hysteresis might appear as unavoidable consequence of the O_2 loss at the first "activation" charge to high voltage, which is also responsible for most of the irreversibility obtained during the first cycle.

To conclude, we have reported the Na-rich $NaLi_{1/3}Mn_{2/3}O_2$ phase having an O3-type structure and showing highly reversible de-insertion/ insertion of ~0.7 Na via combined cationic and anionic redox processes. At a fundamental level, with this material we could consolidate the established link between cation migration and voltage fade, demonstrating that the voltage fade can be arrested by switching migration of the transition metal to an intralayer mode through displacement the Li^+ cations from the $[Li_{1/3}Mn_{2/3}]O_2$ layers to the alkali layers on the first charge. At a practical level, O3-$NaLi_{1/3}Mn_{2/3}O_2$ offers positive attributes such as a reversible capacity of 190 mAh g^{-1} associated with a good capacity retention and no discernable voltage fade while showing robust water stability, which is rare for stoichiometric Na-based layered compounds representing a serious asset for the future applications. Therefore, as the remaining voltage hysteresis in this material still stands as a roadblock, we are trying to solve via the injection of a robust ordering scheme within the transition metal layer. We hope these findings pave the way towards the design of novel moisture stable anionic redox active O3-type Na phases having large capacity and minimized voltage fade and hysteresis for the next generation of advanced Na-ion batteries.

Acknowledgements

Q.W. thanks Renault S.A.S for PhD funding. J.-M.T. acknowledges the funding from European Research Council (ERC) (FP/2014)/ERC Grant-Project 670116-ARPEMA. A.M.A and A.V.M are grateful to Russian Science Foundation for the financial support (grant 20-43-01012). Access to the TEM facilities has been granted by Advance Imaging Core Facility of Skoltech. We thank the ROCK beamline at SOLEIL (Gif-sur-Yvette, France) for X-ray spectroscopy experiments (financed by the French National Research Agency (ANR) as a part of the "Investissements d'Avenir" program, reference: ANR-10-EQPX-45; proposal #20171234 and #20190596). HAXPES measurements were performed at GALAXIES beamline at SOLEIL Synchrotron, France under proposal #20171035 and #20190646. This work used resources of the Advanced Photon Source (11-BM), a U.S. Department of Energy (DOE) Office of Science User Facility operated for the DOE Office of Science by Argonne National Laboratory under Contract No. DE-AC02-06CH11357. NPD measurements were performed using the ECHIDNA instrument at ANSTO (Sydney, Australia). The authors are grateful to A. Iadecola for the help during XAS measurements. The authors thank C. Masquelier, S. Trabesinger, D. Giaume, M.F. Lagadec, W. Yin, A. Perez, B. Li, G. Yan, G. Assat and J. Vergnet for fruitful discussions. The authors acknowledge the staff of the MPBT (physical properties – low temperature) platform of Sorbonne Université for their support.

Author contributions

Q.W, S.M. and J.-M.T. conceived the idea and designed the experiments. M.D. and B.P. performed NMR measurements. J.C./Y.-S.Y., R.D. and J.W./W.Y. performed and interpreted the XANES/EXAFS, HXAPES and mRIXS measurements. M.A. collected the NPD data, G.R. analyzed and interpreted the SXRD and NPD patterns and performed the magnetic measurements while A.V. M and A. A collected and interpreted all the microscopy data. Lastly, L. Z. performed the OEMS measurements and M.C. supervised the project. M-L.D performed the theoretical calculations and contributed to the overall interpretation of the results. J.-M.T, A.A, S.M and Q.W. wrote the paper, with contributions from all authors.

Competing interests

The authors declare no competing interest. The material O3-Na($Li_{1/3}Mn_{2/3}$)O_2 is patented with patent application number B19-5233FR.

References

1. Tarascon, J. M. The Li-Ion Battery: 25 Years of Exciting and Enriching Experiences. *Electrochem. Soc. Interface* **25**, 79–83 (2016).
2. Yabuuchi, N., Kubota, K., Dahbi, M. & Komaba, S. Research Development on Sodium-Ion Batteries. *Chemical Reviews* **114**, 11636–11682 (2014).
3. Hwang, J.-Y., Myung, S.-T. & Sun, Y.-K. Sodium-ion batteries: present and future. *Chemical Society Reviews* **46**, 3529–3614 (2017).
4. Rozier, P. & Tarascon, J. M. Review—Li-Rich Layered Oxide Cathodes for Next-Generation Li-Ion Batteries: Chances and Challenges. *J. Electrochem. Soc.* **162**, A2490–A2499 (2015).
5. Lu, Z. & Dahn, J. R. Understanding the Anomalous Capacity of Li / Li [Ni x Li (1 / 3 − 2x / 3) Mn (2 / 3 − x / 3)] O 2 Cells Using In Situ X-Ray Diffraction and Electrochemical Studies. *J. Electrochem. Soc.* **149**, A815–A822 (2002).
6. M. Thackeray, M., S. Johnson, C., T. Vaughey, J., Li, N. & A. Hackney, S. Advances in manganese- oxide 'composite' electrodes for lithium-ion batteries. *Journal of Materials Chemistry* **15**, 2257–2267 (2005).
7. Xie, Y., Saubanère, M. & Doublet, M.-L. Requirements for reversible extra-capacity in Li-rich layered oxides for Li-ion batteries. *Energy Environ. Sci.* **10**, 266–274 (2017).
8. Ben Yahia, M., Vergnet, J., Saubanère, M. & Doublet, M.-L. Unified picture of anionic redox in Li/Na-ion batteries. *Nature Materials* **18**, 496–502 (2019).

9. Rozier, P. *et al.* Anionic redox chemistry in Na-rich Na2Ru1−ySnyO3 positive electrode material for Na-ion batteries. *Electrochemistry Communications* **53**, 29–32 (2015).
10. Assadi, M. H. N., Okubo, M., Yamada, A. & Tateyama, Y. Oxygen Redox Promoted by Na Excess and Covalency in Hexagonal and Monoclinic Na2−xRuO3 Polymorphs. *J. Electrochem. Soc.* **166**, A5343–A5348 (2019).
11. Mortemard de Boisse, B. *et al.* Intermediate honeycomb ordering to trigger oxygen redox chemistry in layered battery electrode. *Nature Communications* **7**, 11397 (2016).
12. Perez, A. J. *et al.* Strong Oxygen Participation in the Redox Governing the Structural and Electrochemical Properties of Na-Rich Layered Oxide Na2IrO3. *Chem. Mater.* **28**, 8278–8288 (2016).
13. Zhang, X. *et al.* Manganese-Based Na-Rich Materials Boost Anionic Redox in High-Performance Layered Cathodes for Sodium-Ion Batteries. *Advanced Materials* **31**, 1807770 (2019).
14. House, R. A. *et al.* Superstructure control of first-cycle voltage hysteresis in O-redox cathodes. *Nature* **577**, 502–508 (2020).
15. Maitra, U. *et al.* Oxygen redox chemistry without excess alkali-metal ions in Na2/3[Mg0.28Mn0.72]O2. *Nature Chemistry* **10**, 288–295 (2018).
16. Du, K. *et al.* Exploring reversible oxidation of oxygen in a manganese oxide. *Energy Environ. Sci.* **9**, 2575–2577 (2016).
17. Rong, X. *et al.* Anionic Redox Reaction-Induced High-Capacity and Low-Strain Cathode with Suppressed Phase Transition. *Joule* **3**, 503–517 (2019).
18. Bai, X. *et al.* Anionic Redox Activity in a Newly Zn-Doped Sodium Layered Oxide P2-Na2/3Mn1−yZnyO2 ($0 < y < 0.23$). *Advanced Energy Materials* **8**, 1802379 (2018).
19. Bai, X., Iadecola, A., Tarascon, J.-M. & Rozier, P. Decoupling the effect of vacancies and electropositive cations on the anionic redox processes in Na based P2-type layered oxides. *Energy Storage Materials* (2020) doi:10.1016/j.ensm.2020.05.032.
20. Ma, C. *et al.* Exploring Oxygen Activity in the High Energy P2-Type Na0.78Ni0.23Mn0.69O2 Cathode Material for Na-Ion Batteries. *J. Am. Chem. Soc.* **139**, 4835–4845 (2017).
21. Mariyappan, S., Wang, Q. & Tarascon, J. M. Will Sodium Layered Oxides Ever Be Competitive for Sodium Ion Battery Applications? *J. Electrochem. Soc.* **165**, A3714–A3722 (2018).
22. Vinckevičiūtė, J., Radin, M. D. & Van der Ven, A. Stacking-Sequence Changes and Na Ordering in Layered Intercalation Materials. *Chem. Mater.* **28**, 8640–8650 (2016).

23. Xu, J., Liu, H. & Meng, Y. S. Exploring Li substituted O3-structured layered oxides NaLixNi1/3−xMn1/3+xCo1/3−xO2 (x = 0.07, 0.13, and 0.2) as promising cathode materials for rechargeable Na batteries. *Electrochemistry Communications* **60**, 13–16 (2015).
24. Zheng, S. *et al.* Exploring the working mechanism of Li^{+} in O3-type $NaLi_{0.1}Ni_{0.35}Mn_{0.55}O_2$ cathode materials for rechargeable Na-ion batteries. *Journal of Materials Chemistry A* **4**, 9054–9062 (2016).
25. Kim, D. *et al.* Enabling Sodium Batteries Using Lithium-Substituted Sodium Layered Transition Metal Oxide Cathodes. *Advanced Energy Materials* **1**, 333–336 (2011).
26. Kim, D., Cho, M. & Cho, K. Rational Design of $Na(Li_{1/3}Mn_{2/3})O_2$ Operated by Anionic Redox Reactions for Advanced Sodium-Ion Batteries. *Adv. Mater.* **29**, 1701788 (2017).
27. Perez, A. J., Rousse, G. & Tarascon, J.-M. Structural Instability Driven by Li/Na Competition in Na(Li1/3Ir2/3)O2 Cathode Material for Li-Ion and Na-Ion Batteries. *Inorg. Chem.* **58**, 15644–15651 (2019).
28. Assat, G., Delacourt, C., Corte, D. A. D. & Tarascon, J.-M. Editors' Choice—Practical Assessment of Anionic Redox in Li-Rich Layered Oxide Cathodes: A Mixed Blessing for High Energy Li-Ion Batteries. *J. Electrochem. Soc.* **163**, A2965–A2976 (2016).
29. de la Llave, E. *et al.* Improving Energy Density and Structural Stability of Manganese Oxide Cathodes for Na-Ion Batteries by Structural Lithium Substitution. *Chem. Mater.* **28**, 9064–9076 (2016).
30. House, R. A. *et al.* What Triggers Oxygen Loss in Oxygen Redox Cathode Materials? *Chemistry of Materials* **31**, 3293–3300 (2019).
31. Guéguen, A. *et al.* Decomposition of $LiPF_6$ in High Energy Lithium-Ion Batteries Studied with Online Electrochemical Mass Spectrometry. *J. Electrochem. Soc.* **163**, A1095–A1100 (2016).
32. Freiberg, A. T. S., Sicklinger, J., Solchenbach, S. & Gasteiger, H. A. Li2CO3 decomposition in Li-ion batteries induced by the electrochemical oxidation of the electrolyte and of electrolyte impurities. *Electrochimica Acta* **346**, 136271 (2020).
33. Grey, C. P. & Lee, Y. J. Lithium MAS NMR studies of cathode materials for lithium-ion batteries. *Solid State Sciences* **5**, 883–894 (2003).
34. Lee, Y. J. & Grey, C. P. Determining the Lithium Local Environments in the Lithium Manganates LiZn0.5Mn1.5O4 and Li2MnO3 by Analysis of the 6Li MAS NMR Spinning Sideband Manifolds. *J. Phys. Chem. B* **106**, 3576–3582 (2002).

35. Shimoda, K. *et al.* Direct observation of layered-to-spinel phase transformation in Li2MnO3 and the spinel structure stabilised after the activation process. *J. Mater. Chem. A* **5**, 6695–6707 (2017).
36. Xu, J. *et al.* Identifying the Critical Role of Li Substitution in P2–Nax[LiyNizMn1–y–z]O2 (0 < x, y, z < 1) Intercalation Cathode Materials for High-Energy Na-Ion Batteries. *Chem. Mater.* **26**, 1260–1269 (2014).
37. Clément, R. J. *et al.* Direct evidence for high Na^+ mobility and high voltage structural processes in P2-$Na_x[Li_y Ni_z Mn_{1-y-z}]O_2$ (x, y, z ≤ 1) cathodes from solid-state NMR and DFT calculations. *J. Mater. Chem. A* **5**, 4129–4143 (2017).
38. Cabana, J. *et al.* Study of the Transition Metal Ordering in Layered NaxNix/2Mn1–x/2O2 (2/3 ≤ x ≤ 1) and Consequences of Na/Li Exchange. *Inorg. Chem.* **52**, 8540–8550 (2013).
39. Assat, G. *et al.* Fundamental interplay between anionic/cationic redox governing the kinetics and thermodynamics of lithium-rich cathodes. *Nat Commun* **8**, 2219 (2017).
40. Dai, K. *et al.* High Reversibility of Lattice Oxygen Redox Quantified by Direct Bulk Probes of Both Anionic and Cationic Redox Reactions. *Joule* **3**, 518–541 (2019).
41. Ito, A. *et al.* In situ X-ray absorption spectroscopic study of Li-rich layered cathode material Li[Ni0.17Li0.2Co0.07Mn0.56]O2. *Journal of Power Sources* **196**, 6828–6834 (2011).
42. Dau, H., Liebisch, P. & Haumann, M. X-ray absorption spectroscopy to analyze nuclear geometry and electronic structure of biological metal centers—potential and questions examined with special focus on the tetra-nuclear manganese complex of oxygenic photosynthesis. *Anal Bioanal Chem* **376**, 562–583 (2003).
43. Croy, J. R. *et al.* First-Cycle Evolution of Local Structure in Electrochemically Activated Li2MnO3. *Chem. Mater.* **26**, 7091–7098 (2014).
44. Vergnet, J., Saubanère, M., Doublet, M.-L. & Tarascon, J.-M. The Structural Stability of P2-Layered Na-Based Electrodes during Anionic Redox. *Joule* **4**, 420–434 (2020).
45. Sathiya, M. *et al.* Origin of voltage decay in high-capacity layered oxide electrodes. *Nature Mater* **14**, 230–238 (2015).
46. Taylor, Z. N. *et al.* Stabilization of O–O Bonds by d^0 Cations in $Li_{4+x} Ni_{1-x} WO_6$ ($0 \leq x \leq 0.25$) Rock Salt Oxides as the Origin of Large Voltage Hysteresis. *J. Am. Chem. Soc.* **141**, 7333–7346 (2019).
47. Jacquet, Q. *et al.* Charge Transfer Band Gap as an Indicator of Hysteresis in Li-Disordered Rock Salt Cathodes for Li-Ion Batteries. *J. Am. Chem. Soc.* **141**, 11452–11464 (2019).

48. Assat, G., Glazier, S. L., Delacourt, C. & Tarascon, J.-M. Probing the thermal effects of voltage hysteresis in anionic redox-based lithium-rich cathodes using isothermal calorimetry. *Nature Energy* **4**, 647–656 (2019).
49. Gent, W. E. *et al.* Coupling between oxygen redox and cation migration explains unusual electrochemistry in lithium-rich layered oxides. *Nat Commun* **8**, 1–12 (2017).
50. Croy, J. R., Balasubramanian, M., Gallagher, K. G. & Burrell, A. K. Review of the U.S. Department of Energy's "Deep Dive" Effort to Understand Voltage Fade in Li- and Mn-Rich Cathodes. *Acc. Chem. Res.* **48**, 2813–2821 (2015).
51. Eum, D. *et al.* Voltage decay and redox asymmetry mitigation by reversible cation migration in lithium-rich layered oxide electrodes. *Nature Materials* **19**, 419–427 (2020).
52. Berg, E. J. & Novák, P. Recent progress on Li-O2 batteries at PSI. in *ECL Annual Report* (Paul Scherrer Institut, Villigen, Switzerland, 2012).
53. Lepoivre, F., Grimaud, A., Larcher, D. & Tarascon, J.-M. Long-Time and Reliable Gas Monitoring in Li-O2 Batteries via a Swagelok Derived Electrochemical Cell. *J. Electrochem. Soc.* **163**, A923–A929 (2016).
54. FullProf Suite Homepage. https://www.ill.eu/sites/fullprof/.
55. Casas-Cabanas, M., Reynaud, M., Rikarte, J., Horbach, P. & Rodríguez-Carvajal, J. FAULTS: a program for refinement of structures with extended defects. *J Appl Cryst* **49**, 2259–2269 (2016).
56. Avdeev, M. & Hester, J. R. ECHIDNA: a decade of high-resolution neutron powder diffraction at OPAL. *J Appl Cryst* **51**, 1597–1604 (2018).
57. Rodríguez-Carvajal, J. Recent advances in magnetic structure determination by neutron powder diffraction. *Physica B: Condensed Matter* **192**, 55–69 (1993).
58. Grandinetti, P. J. *et al.* Pure-Absorption-Mode Lineshapes and Sensitivity in Two-Dimensional Dynamic-Angle Spinning NMR. *Journal of Magnetic Resonance, Series A* **103**, 72–81 (1993).
59. Massiot, D. *et al.* Modelling one- and two-dimensional solid-state NMR spectra. *Magnetic Resonance in Chemistry* **40**, 70–76 (2002).
60. Rueff, J.-P. *et al.* The GALAXIES beamline at the SOLEIL synchrotron: inelastic X-ray scattering and photoelectron spectroscopy in the hard X-ray range. *J Synchrotron Rad* **22**, 175–179 (2015).
61. Qiao, R. *et al.* High-efficiency in situ resonant inelastic x-ray scattering (iRIXS) endstation at the Advanced Light Source. *Review of Scientific Instruments* **88**, 033106 (2017).

62. Briois, V. *et al.* ROCK: the new Quick-EXAFS beamline at SOLEIL. *J. Phys.: Conf. Ser.* **712**, 012149 (2016).
63. Kresse, G. & Hafner, J. Ab initio molecular dynamics for liquid metals. *Phys. Rev. B* **47**, 558–561 (1993).
64. Kresse, G. & Furthmüller, J. Efficiency of ab-initio total energy calculations for metals and semiconductors using a plane-wave basis set. *Computational Materials Science* **6**, 15–50 (1996).
65. Perdew, J. P., Burke, K. & Ernzerhof, M. Generalized Gradient Approximation Made Simple. *Phys. Rev. Lett.* **77**, 3865–3868 (1996).
66. Dudarev, S. L., Botton, G. A., Savrasov, S. Y., Humphreys, C. J. & Sutton, A. P. Electron-energy-loss spectra and the structural stability of nickel oxide: An LSDA+U study. *Phys. Rev. B* **57**, 1505–1509 (1998).

Methods

Synthesis. 415 mg of Na_2O_2 (Alfa Aesar, 95%), 53 mg of Li_2O (Alfa Aesar, 99.5%) and 560 mg of Mn_2O_3 (Sigma Aldrich, 99%) were thoroughly mixed in a mortar prior to be placed in an alumina boat. The boat was placed in a quartz tube of 62 cm length and 32 mm diameter that was placed in a tubular furnace (type carbolite) having a 30 cm heating zone. After placing the sample, the alumina tube was flushed with argon for 45 minutes with an Ar flow of 50mL/ min. Then, the argon flow was stopped and the sample was heated to 700 °C for 8h and then cooled down to room temperature. The as-synthesized material was soaked in distilled water (100 mg/10 mL H_2O) while sonicating for 30 minutes followed by drying at 80 °C under vacuum overnight.

Electrochemical characterization. Electrochemical characterization was carried out in Swagelok-type cells versus metallic Na, with 1 M $NaPF_6$ (Stella Chemifa) dissolved in propylene carbonate (PC) as electrolyte, and Whatman GF/D borosilicate glass fiber membrane as separator. The cathode material was used in form of self-standing film electrode comprising 76 wt% active material, 20 wt% carbon Super P (Csp) and 4 wt% polytetrafluoroethylene (PTFE). Typical loading of cathode active materials was around 5 mg/cm^2. All cells were assembled in an Ar-filled glovebox and were cycled in galvanostatic mode at current rates ranging from C/8 to C/20 (1 Na^+ exchanged in 8 to 20 hours). Galvanostatic intermittent titration technique (GITT) measurement was performed in the second cycle of $NaLi_{1/3}Mn_{2/3}O_2$/Na cells at 25 °C with steps of 0.2 Na^+ exchange and OCV period of 20 h.

For cycling versus metallic Li, a nearly Na-free electrode, $Na_{0.09}Li_{1/3}Mn_{2/3}O_2$ was recovered and washed from a $NaLi_{1/3}Mn_{2/3}O_2$/Na Swagelok cell that was fully charged to 4.5 V vs Na^+/Na^0, prior to being used in a new Swagelok with Li metal as a negative electrode and 1M $LiPF_6$ in EC-DMC (v/v = 50/50) as electrolyte. The Li cells are also cycled at current rates ranging from C/8 to C/20 at 25 °C.

To prepare *ex situ* samples for characterization, the cathode consisted of either PTFE film (XAS, mRIXS) as described before, or a powder composite of active material mixed with 15−25 wt% Csp (SXRD, TEM, NMR, HAXPES, SQUID, ICP). *Ex situ* samples were extracted from the cycled cells in an Ar-filled glovebox and washed in anhydrous dimethyl carbonate (DMC) for five times before sealing and transferring under Ar.

Gas analysis. For pressure analysis and OEMS measurements, we employed $Na_3V_2(PO_4)_3$ as counter electrode to avoid gas generation from side reactions with common anode materials such as Na and hard carbon. The $NaLi_{1/3}Mn_{2/3}O_2$ and $Na_3V_2(PO_4)_3$ (NVP) were used both in form of self-standing electrode (76% active material, 20% Csp, 4% PTFE). One piece of GF/D glass fiber was used as separator. In-house pressure cells or OEMS cells were assembled in an Ar-filled glovebox and then cycled at C/20 current rate (0.05 Na^+ exchange/h for $NaLi_{1/3}Mn_{2/3}O_2$) with 150 µL of electrolyte (1 M $NaPF_6$ dissolved in PC) and cut-off potentials of – 0.5–3.1 V vs. NVP. The OEMS and pressure cell setup was described elsewhere.[52,53] For OEMS, gaseous products were collected and analyzed by LabView program.

XRD. XRD patterns were performed on pristine samples using a BRUKER D8 Advance diffractometer equipped with Cu Kα radiation source (λ Kα_1 = 1.54056 Å, λ Kα_2 = 1.54439 Å). *Operando* XRD was carried out on the same diffractometer in an electrochemical cell equipped with a Be window. SXRD was performed on pristine and *ex situ* powders at the 11-BM beamline (Advanced Photon Source, Argonne National Laboratory). Rietveld refinement on the XRD patterns were conducted using FullProf Suite.[54] Simulation of stacking faults in the pristine sample was done with the FAULTS software available in the FullProf Suite.[55]

TEM. The samples were prepared by crushing the crystals with an agate mortar and pestle in dimethyl carbonate and depositing drops of suspension onto a carbon film supported by a copper grid. Samples for TEM were stored and prepared in an Ar-filled glovebox. A special Gatan vacuum transfer holder was used for analyses and transportation of the samples from the Ar-filled glovebox to the TEM column to prevent the interaction with air. Selected area electron diffraction (SAED) patterns and high resolution high angle annular dark field scanning transmission electron microscopy (HAADF-STEM) images were acquired on a probe aberration-corrected FEI Titan Themis Z transmission electron microscope operated at 200 kV.

NPD. Neutron diffraction data were collected at the ECHIDNA high-resolution powder diffractometer at the OPAL research facility (Lucas Heights, Australia).[56] Three samples were filled into thin-wall vanadium containers with the wall thickness (150 µm) and 10 mm in diameter and sealed under argon with indium metal wire. The data collection was performed at ambient temperature in Debye-Scherrer geometry under constant spinning. Monochromatic neutrons were obtained at (533) reflection of composite vertically focusing Ge

monochromator at 140° take-off angle. Wavelength λ = 1.622043(15) Å was determined using the full-profile refinement of LaB_6 reference from NIST. Diffraction data were obtained in the 2θ range (4-164 deg) using 25 resolution steps of the 2D multidetector consisting of 128 ^{3}He vertically positionally sensitive tubes. The exposure time was 9 h per dataset and equal for the samples studied. All patterns were refined by Rietveld method using the FullProf suite.[57]

ICP. ICP was performed to determine the elemental compositions of the material before and after H_2O treatment and electrochemical cycling with a ThermoFisher iCAP 6000 device. All powders were first digested in aqua regia, followed by a filtering process for the cycled samples to remove the conductive carbon in the composite electrodes.

NMR. Solid-state NMR experiments were performed on a 4.7 T Avance III HD Bruker NMR spectrometer (200 MHz for ^{1}H, 29.4 MHz for ^{6}Li and 52.9 MHz for ^{23}Na), using a 1.3 mm MAS probe spinning at 62.5 kHz under pure nitrogen gas. Without temperature regulation, the temperature inside the rotor is expected to be around 50°C.

All experiments were recorded with a rotor-synchronized Hahn echo sequence. For the ^{6}Li spectra, the 90° pulse was set to 1.11 μs and the chemical shift was referenced with liquid ^{6}LiCl in water (corresponding to a 225 kHz B_1 field strength). For ^{23}Na spectra, the Hahn echo was recorded with a 45°−τ−90°−τ sequence to account for the quadrupolar effect, using a 1.47 μs long, low power 45° radiofrequency pulse (corresponding to a 85 kHz B_1 field strength). To ensure optimal detection of the signals affected by quadrupolar broadening, several experiments were performed with RF powers ranging between 50 and 5W, and the RF power was set at 12.5W to avoid any loss of signal. Moreover, to ensure proper detection and phasing of the broad signal for discharged samples and avoid baseline distortion issues, a full echo signal was also acquired after a first evolution delay of 16 rotor periods[58]. The resulting full echo signal has the same lineshape as the conventional Hahn echo signal after proper phasing, thereby confirming the first results. All T_1 relaxation times were measured in the 500 μs – 10 ms range, and therefore, all spectra were recorded with a 50 ms recycling delay ensuring full recovery of the magnetization. No spinning sideband were detected in our experiments thanks to the low-field/high spinning speed combination.

The 1.3 mm zirconia rotor were filled inside a glove box under argon, and the rotor was weighted before and after the filling procedure to obtain the sample mass (around 2.7 to 4.6 mg). Depending upon the sensitivity of the experiments, the total number of recorded

transients varied between 32’768 and 1’403’472 and MAS was performed under dry N_2 gas. The spectra were deconvoluted with dmfit.[59] Special care was taken to measure NMR spectra on fresh samples with as little contact as possible with residual moisture in the glove box or in the NMR spectrometer. Contact with moisture results in the quick evolution of the NMR spectra, with sharper peaks appearing in the 0-300 ppm range in ^{23}Na NMR spectra, as noticed previously[37].

HAXPES. HAXPES measurements were performed at the GALAXIES beamline of synchrotron SOLEIL (France),[60] using photon excitation energy of $h\upsilon$ = 6900 eV obtained from the third-order reflections of the Si(111) crystal monochromator. Photoelectrons were analyzed by a SCIENTA EW4000 spectrometer, and the obtained energy resolution from the Au Fermi edge was 0.14 eV for 6900 eV photon energy. No charge neutralization was used and the analysis chamber was under high vacuum of ~ 10^{-11} bar during the measurements.

mRIXS. mRIXS was measured in the iRIXS endstation at Beamline 8.0.1 of Advanced Light Source, Lawrence Berkeley Lab.[61] Further experimental details are exhibited in supplementary note 1.

XAS. *Ex situ* and *operando* XAS measurements at the Mn K-edge were performed in transmission mode at the ROCK beamline[62] of synchrotron SOLEIL (France). Further details of the experiments and data analyses are included in supplementary note 2.

Magnetic measurements. Susceptibility measurements were conducted in zero field cooling (ZFC) mode using a SQUID XL magnetometer (Quantum design), under applied magnetic fields of 1 T in temperature range of 2−400 K. The powder samples were sealed in quartz tubes under vacuum to avoid any contact with air. A small piece of cotton is used to prevent the motion of the powders along the quartz tube. Both the quartz tube and cotton are found to be transparent to magnetic measurements.

DFT. Spin-polarized density functional theory (DFT) calculations were performed using the plane-wave density functional theory VASP (Vienna Ab initio Simulation Package) code[63,64] within the generalized gradient approximation of Perdew–Burke–Ernzerhof (PBE) to describe electron exchange and correlation.[65]

The rotationally invariant Dudarev method (DFT+U)[66] was used to correct the self-interaction error of conventional DFT for correlated d-electrons with U_{eff} = 4 eV for Mn. Various Li/Na configurations were tested with alkali lying in the 2*b*, 2*c* or 4*h* Wyckoff positions of the *C*2/*m*

model structure. Mn migration was investigated in 2×1×1 super-cells (8 Mn per cell). All atom coordinates and lattice parameters were fully relaxed using conjugate gradient energy minimization until the forces acting on each atom were less than 5.10^{-3} eV Å^2. A plane-wave cutoff of 600 eV was used to define the basis set, with well-converged k-point sampling for each compound. Both ferromagnetic and antiferromagnetic arrangements were considered in the calculation, the former leading generally to slightly more stable structures within one or two k_BT (room temperature activation energy ~25 meV). Madelung potentials were computed using home-made code.